LAWRENCE
LIVERMORE
NATIONAL
LABORATORY

LLNL-JRNL-654740

An Experimental Investigation into Additive Manufacturing Induced Residual Stresses in 316L Stainless Steel

A. S. Wu, D. W. Brown, M. Kumar, G. Gallegos, W. E. King

May 21, 2014

Metallurgical and Materials Transactions A

Disclaimer

An experimental investigation into additive manufacturing induced residual stresses in 316L stainless steel

Amanda S. Wu[1], Donald W. Brown[2], Mukul Kumar[1], Gilbert F. Gallegos[1], and Wayne E. King[3]

[1]Materials Engineering Division, Lawrence Livermore National Laboratory, 7000 East Avenue, Livermore, CA 94550, USA
[2]Materials Science & Technology Division, Los Alamos National Laboratory, PO Box 1663, Los Alamos, NM 87545, USA
[3]Condensed Matter and Materials Division, Lawrence Livermore National Laboratory, 7000 East Avenue, Livermore, CA 94550, USA

Abstract

Additive manufacturing (AM) technology provides unique opportunities for producing net-shape geometries at the macroscale through microscale processing. This level of control presents inherent trade-offs necessitating the establishment of quality controls aimed at minimizing undesirable properties, such as porosity and residual stresses. Here, we perform a parametric study into the effects of laser scanning pattern, power, speed, and build direction in powder bed fusion AM on residual stress. In an effort to better understand the factors influencing macroscale residual stresses, a destructive surface residual stress measurement technique (digital image correlation in conjunction with build plate removal and sectioning) has been coupled with a nondestructive volumetric evaluation method (i.e., neutron diffraction). Good agreement between the two measurement techniques is observed. Furthermore, a reduction in residual stress is obtained by decreasing scan island size, increasing island to wall rotation to 45º and increasing applied energy per unit length (laser power/speed). Neutron diffraction measurements reveal that, while in-plane residual stresses are affected by scan island rotation, axial residual stresses are unchanged. We attribute this in-plane behavior to misalignment between the greatest thermal stresses (scan direction) and largest part dimension.

Introduction

Additive manufacturing (AM) refers to a family of layer-by-layer building methodologies capable of producing three-dimensional structures from a precursor material[1,2]. While the focus of this work is on metal-based powder bed fusion additive manufacturing, AM methods have found applications in metals[3], polymers, and ceramics[4,5] due to their ability to create complex, net shape parts with little waste material using a single automated process. Despite over two decades of AM technology, significant challenges for large-scale incorporation of AM methodologies remain. Inherent trade-offs between achieving fast processing times, full-density, relatively stress free structures and good microstructural and mechanical integrity have created a demand for process optimization.

In powder bed fusion AM, a very thin powder layer is distributed and selectively melted by a controlled laser; this procedure is repeated until a complete part is built. Powder size and packing, material, laser settings (power, spot size, speed) and scanning parameters (pattern, orientation angle, overlaps) must be selected such that the powder layer is fully melted locally and bonded to the substrate. However, the development of large thermal gradients near the laser spot[6], rapid cooling and repetition of this process gives rise to localized compression and tension, resulting in AM parts with significant residual stresses. The thermal gradients present during

building are affected by many process parameters (part size, build time, build plate/powder bed temperature, atmosphere, powder thermal characteristics, melt pool size, etc.). Aside from their potential impact on the mechanical performance and structural integrity of AM parts, residual stresses developed during processing may cause localized deformations resulting in a loss of net shape, detachment from support structures, or failure of the AM part.

Parametric effects on residual stress

The growing importance of AM technologies in industry calls for a concentrated, systematic effort to understand the effect of and coupling between each component in the powder bed fusion AM parameter space with residual stress development. However, the confounding behavior inherent in parameter optimization for full density, microstructure/mechanical performance and residual stress must not be neglected.

It is a well-documented fact that powder bed fusion AM processing can lead to residual stresses as high as the bulk yield strength of the AM material[6] and, sometimes, in excess of such[7]. Due to limitations in available laser power settings, rather than investigate melt-pool-size related effects on residual stress, recent experimental efforts focused on minimizing residual stresses by tailoring the laser scanning pattern. The reduction in residual stresses with the use of shorter scan lines[8], scan vector reduction[9] and island scanning (which can result in a 40% reduction in residual stress[10]) has been well-documented. The potential to minimize residual stresses by altering scanning orientation exists[8,9] and laser path optimization based on inherent substrate (i.e., build plate) preheating has been proposed and demonstrated by Klingbeil et al.[11].

Since residual stresses are such an undesirable phenomenon in AM processing, many studies into their characterization have prompted the development of process modifications aimed at their mitigation. While in situ heating (e.g., build plate heating; reheating of the melt pool) has been shown to reduce residual stresses in AM parts[12,13], a more common approach is ex situ annealing[14], which has demonstrated a 70% reduction in residual stresses.

Residual stress measurement methodologies

Residual stress measurements can be categorized as either nondestructive[15] or destructive; both categories have benefits and drawbacks and tend to be application specific[16]. The most commonly used nondestructive methods are X-ray[17] and neutron diffraction[18], which are capable of providing near-surface and volumetric residual stress measurements in crystalline materials, respectively[19]. These methods provide accurate residual stress measurements without the need for numerical analysis (e.g., finite element analysis (FEA)) yet require specialized equipment (i.e., synchrotron or neutron sources). Other nondestructive methods include ultrasonics[20], electrical resistivity[21], magnetic behavior[22], and piezo-spectroscopy in thin films[23,24]; these are material and geometry specific. While these methods are largely used ex situ, X-ray diffraction has been used to evaluate other types of process-induced residual stresses in situ (thin films[25], welded materials[26] and composites[27]).

Destructive methods mainly revolve around creating free surfaces in a part and relating resultant deformations back to residual stresses (e.g., hole drilling[28], sectioning or contouring[29] and crack compliance or slitting[30]). Aside from traditional strain gages, newer, whole-surface measurement methods have been used in this endeavor, including digital image correlation (in conjunction with hole drilling[31-34], before-and-after thermal coating application[35] and even focused ion milling[36-38]) and electronic speckle pattern interferometry (ESPI) (in conjunction with hole

drilling[39-42]. Indentation[43] has been used to measure surface-level residual stresses as well. While destructive methods are capable of providing location-specific residual stress information, they typically require the use of additional analysis (e.g., FEA) to determine residual stresses from deformation behavior.

Qualitative evaluations are often practical, given the large parameter space and need for comparison among AM parts (e.g., process-induced warping[11] and the bridge method/warping upon build plate removal[9,44]. These indirect methods provide a parameter (i.e., deflection angle) which is used as a basis for comparison of various AM parts without the need for FEA.

In this study, we explored the ability of DIC used in conjunction with sectioning to provide quantitative, surface-level residual stress measurements (also without FEA) in thick section parts and validated this approach using near-surface measurements made via neutron diffraction. DIC was selected due to its ability to obtain fast, accurate, non-contact surface measurements without surface conditioning. Neutron diffraction provided accurate, nondestructive internal residual strain measurements. These experimental techniques were performed to (1) demonstrate the ability of DIC to function as a residual stress measurement technique, (2) measure quantitatively the residual stress distributions and relate such to deformation behavior upon sectioning/build plate removal, (3) understand the effect of laser scanning pattern, power, and speed on residual stresses in AM 316L stainless steel and (4) draw conclusions on the factors influencing residual stresses in powder bed fusion AM parts.

Materials and Methods

Specimen Preparation

All AM specimens were processed using 316L stainless steel powder (Concept Laser, CL-20) with a 30 µm powder layer. L-shaped rectangular and quadrilateral prism (Fig. 1) specimens were built using a Concept Laser M2 (50 µm, D4Sigma Gaussian beam) with power and speed parameters selected based on a density optimization study by Kamath et al.[45]. The L-shaped specimens were designed to facilitate neutron diffraction measurements; additionally, they possess interesting in-plane and axial residual stress gradients. Prism specimens were selected to highlight the effect of length scale on residual stress development. The 5 x 5 mm island scanning strategy, patented by Concept Laser GmbH, and discussed by Kruth et al.[11] was adopted in the preparation of the L-shaped specimens. In the case of the prisms, scanning pattern was varied between a continuous scan (perpendicular to the base, in the case of horizontally-built specimens, with scan lines overlapping), 3 x 3 mm islands, and 5 x 5 mm islands (with a hatch angle perpendicular to the base in both cases).

Mechanical Behavior and Porosity

Laser-based additive manufacturing gives rise to non-homogeneous morphologies and, sometimes, anisotropic[46] grain structures often with some degree of porosity. The microstructure of 316L stainless steel specimens processed at 400W using different scanning strategies is shown in Fig. 2. Here, the dark spots represent pores formed during processing. Melt pool lines non-epitaxial growth is evident in Fig. 2c and Fig. 2f.

In order to accurately calculate residual stresses based on measured deformations/strains, it is necessary to characterize the bulk mechanical properties of AM specimens. AM metals often exhibit higher-than-average yield stresses[47], likely due to the nucleation of dislocations driven by

the extreme stresses induced during processing (consequent melting/expansion and solidification/shrinking). The elastic modulus, yield stress and porosity have been measured respectively via resonance ultrasound spectroscopy (RUS), mechanical axial compressive loading and Archimedes' Principle in conjunction with image analysis, respectively, as a function of scanning pattern (Table 1). Small specimens (0.5 cm) were evaluated in order to minimize any residual stress-related measurement artifacts.

Elastic modulus measurements are used in the following sections to calculate residual stresses from DIC measured strains. Note that elastic modulus decreases with porosity in an expected manner. An extensive review of porosity-elastic modulus relationships can be found in the manuscript by Choren et al.[48].

L-shaped specimens built at various laser power and speed settings yielding porosity values <1.5% (Table 2). Since laser power and speed are coupled, it is beneficial to use a single parameter to describe the overall effect of each power/speed setting explored. We have considered volumetric energy density[49] and normalized enthalpy (Eq. 1)[50]. However, the former does not account for beam size, while the latter requires accurate measurements of thermal properties, which are not currently available. The melt pool geometry for each laser power/speed setting of interest has also been estimated using the Eager-Tsai model[51]. These parameters are reported in Table 2; however, the most straightforward method for comparison consisting of the least number of assumptions is energy per unit length (laser power divided by speed).

$$\frac{\Delta H}{h_s} = \frac{\eta P}{\rho h_s \sqrt{\pi \alpha \sigma^3 U}} \qquad \text{Eq. 1}$$

Neutron Diffraction

Neutron diffraction measurements were performed on the SMARTS diffractometer at the Lujan Center at the Los Alamos Neutron Science Center (LANSCE), Los Alamos National Laboratory, following the procedure described in detail by Brown et al.[18].

Digital Image Correlation

In an effort to characterize the surface residual stresses affecting the specimens described above, a modified contour method has been adopted. A non-contact optical measurement system (ARAMIS, GOM mbH) was used to evaluate the strain resulting from sectioning and build plate removal. This analysis is performed by digitally comparing images acquired before and after localized stress relief due to sectioning. Specifically, a black and white speckle pattern is applied to the AM specimen, which enables the ARAMIS software to divide an image of the part into a specified number of facets. Localized deformation of these facets is measured and used to calculate the strain components over facets across the part. The stress giving rise to the observed strain is representative of the surface-level residual stresses in the specimen, local to the cut surface.

A facet size of 100 pixels was found to provide optimal displacement measurements with minimal edge loss (based on a calculation matrix of 5x5 facets) for our speckled AM specimens. These parameters yielded a maximum noise of <0.03% strain. Noncontact wire EDM was used for all sectioning in order to prevent localized plastic deformation typically introduced through conventional machining[29]; however, this method has been shown to induce localized tensile residual stresses up to a maximum depth of 50 μm in C45 steel[53]. Despite this, wire EDM is

considered a standard for stress-relieving residual stress measurement techniques, as deformations arising from sectioning-induced strain relief in AM parts are observed to be about 60 times larger than the surface wire EDM interaction layer.

Results and Discussion

Residual Stress

1. Prism surface displacements

Digital image correlation in conjunction with sectioning and build plate removal was used in an effort to evaluate the effect of build direction and scanning strategy on residual stress development in 316L stainless steel specimens built at a laser power and speed setting of 400W and 1800mm/s, respectively. Both "horizontally"- (z-direction) (Fig. 3) and "vertically"-built (y-direction) (Fig. 4) specimens experienced spherical deflection upon build plate removal, with edges "peeling up" away from the plate. Specifically, in horizontal builds, shrinking in x (Fig. 3a) and y (Fig. 3b), accompanied by spherical deflection in z is observed.

The lower 2 cm of vertically-built specimens (Fig. 4) experiences deformation upon build plate removal. Specifically, expansion in x (Fig. 4a) near the base and contraction in the bottom half of the prism is observed. This behavior, coupled with the positive bending moment in y (Fig. 4b) points to similar spherical deformation local to the base of the specimen. The lack of displacement at the top half of the specimen does not imply that there are zero residual stresses in this region; rather, it is a feature of the specimen's ability to self-relieve elastically upon the removal of a constraint.

2. Prism internal strains

Neutron diffraction scans (Fig. 5) indicate significant in-plane (σ_{xx} and σ_{yy}) residual stresses near the top of the prism, which abate near the stress-relieved face (base). The axial (Fig. 5b) residual stresses also abate near the base; however, there is a significant tensile component on one side of the specimen. This asymmetry could either be attributed to post-processing surface preparation (polishing) on this face or a bending moment within the vertical specimen.

3. L-shaped specimen DIC and neutron diffraction measurements

To better understand the in-plane residual stress distributions established during powder bed fusion AM, neutron diffraction measurements of an L-shaped specimen (400W, 1800mm/s, 5x5 mm island pattern at 45º to the part edge) are provided as a function of position in Fig. 6. Near the top surface of the part (Fig. 6a-6c), significant axial residual stresses are present. In-plane residual stresses are greatest along the largest part geometry—σ_{xx} in the x-direction and σ_{yy} in the y-direction. The evolution of the in-plane residual stress from high (Fig. 6b) to lower and near-zero (Fig. 6e) tensile values translates into the "peeling away" (downward curvature when observed from the top surface) observed upon horizontal sectioning of these parts.

The axial residual stress gradient becomes well-established at 15 mm height (Fig. 6f); note that residual stresses are compressive at the center of each arm and tensile at the corners with the exception of the interior corner. We observe this to be typical in our as-processed powder bed fusion AM structures.

A composite cross-section has been compiled based on stresses calculated from neutron diffraction and DIC-measured displacements (Fig. 7a) acquired at mid-height in an L-shaped specimen. The combination of methods provides a complete view of surface and volumetric axial residual stresses. This is important due to the significant variation in residual stress, which is highly compressive near the center of the part and highly tensile at corners (Fig. 7b). A notable exception is the interior corner, which possesses near-zero axial (σ_{zz}) residual stresses, providing a good example of the effect that part geometry can have on residual stress development.

Axial (σ_{zz}) neutron diffraction scans were performed in three locations along this corner region (Fig. 8). Here, it is evident that axial strains (ε_z) are largest near the build plate, near-zero at the top free surface, and vary from tensile to compressive as a function of distance from exterior corner and from the build plate.

4. Scan strategy

4.1 Island size

Significant tensile stresses are observed at the surface of AM parts (Fig. 9); this is in agreement with the findings of Mercelis and Kruth[6], in which sector scanning strategies aimed at reducing the large tensile residual stresses in the top portion of the part are discussed. A decrease in tensile residual stresses upon reducing the island size from 5 x 5 mm to 3 x 3 mm is observed. Kruth et al.[9] observed qualitatively that a reduction in scan vector length resulted in a reduction of curling angle in bridge-like specimens upon build plate removal, concluding that residual stresses were lower for smaller scan vectors. While their analysis did not capture an effect of decreasing island size, these results are consistent with their findings on scan vector length. Lower tensile residual stress observed in the continuously scanned prism specimen is attributed to self-relieving due to significant internal free surfaces (high porosity), as well as the lower effective elastic modulus measurement used in the calculation of residual stresses from DIC measured strains.

Measurements of tensile residual stresses in excess of yield have been reported for AM specimens previously[7]. Here, we make the assertion that bulk yield strength measurements may not be appropriate for comparison with residual stresses in AM parts, which are non-uniform and thus expected to affect bulk yield strength measurements.

4.2 Island rotation

A comparison of residual strains within the 9 mm arm of three L-shaped specimens is provided in Fig. 10. Observe that island orientation/power/speed affect the in-plane strain components (ε_x and ε_y), while axial strains (ε_z) remain unaffected. Specifically, a significant decrease in tensile residual strains in the y-direction is apparent between specimens built at 400 W, 1800 mm/s and 250 W, 1800 mm/s. Rather than attribute this phenomenon to an increase in laser power, we attribute it to island rotation from 0º to 45º from the part wall. This conclusion is in agreement with the results of the qualitative residual stress evaluation performed by Kruth et al.[9]. We attribute this in-plane behavior to misalignment between the greatest thermal stresses (scan direction) and largest part dimension. By contrast, the axial thermal gradients are unaffected by island rotation and remain controlled by laser settings/enthalpy, geometry and boundary conditions.

5. Laser power

The effects of laser settings are less straightforward to evaluate than scanning strategy, due to their numerous and coupled effects. At a given laser power, fast scanning will result in insufficient melting and poor density while too slow scanning will result in overheating and keyholing[45], which leads to voids in sub-surface layers and, once again, poor density. These parameters also affect thermal gradients, cooling rates and build time, all of which affect residual stress development. Therefore, understanding their contribution is critical in process optimization. However, there are few studies aimed at such[54] and less which evaluate laser powers greater than 200W.

A qualitative assessment can be made using the DIC measured deflection of an exposed surface within these parts. A decrease in residual stress-induced deflection is observed in parts built at increasing energy per unit length, with the least amount of deflection occurring in parts built at a laser power and speed of 100 W and 400 mm/s, respectively. Furthermore, this approach confirms the role of island rotation in reducing residual stresses in parts built at 400 W and 1800 mm/s.

Conclusions

A digital image correlation based method for measuring surface level residual stresses is presented and used in conjunction with neutron diffraction to assess the effect of specimen geometry and AM parameters, specifically scanning pattern and laser power/speed, on residual stress development. Combined stress-relief-via-sectioning and digital image correlation provide surface residual stress measurements without surface conditioning or finite element analysis. Results obtained using this approach are in good agreement with near-surface neutron diffraction measurements made on the same part (Fig. 7), thus demonstrating the ability of this method to provide not only qualitative insight into process-induced residual stresses (Fig. 11), but also quantitative surface level residual stress measurements (Fig. 9).

Powder bed fusion AM results in residual stresses which, in the absence of annealing, cause spherical deformation upon sectioning/build plate removal in the prism and L-shaped specimens studied herein. This deformation is highly pronounced in horizontally-built prism specimens and is more localized in vertically-built prisms. Findings of this study are consistent with the literature in that residual stresses generated during AM processing tend to be compressive near the center of AM specimens and tensile near surfaces[6] and that scan vector length and island rotation[9] play a significant role in residual stress development. Experimental observations on the effects of processing parameters are summarized below.

1. A decrease in tensile residual stresses is observed for specimens built using 3x3 mm islands (as compared with 5x5 mm islands). Further reduced residual stresses are observed for continuously scanned prisms (Fig. 10)—this is attributed to a significant quantity of pores introduced during processing (Fig. 2b), which aid stress relief and decrease elastic modulus (thus reducing calculated residual stress).
2. Neutron diffraction measurements reveal that in-plane residual strains are affected by island rotation, while axial residual strains remain unchanged. We assert that this reduction in residual stresses through the use of 45° off-axis scanning creates a beneficial misalignment between the greatest thermal stresses (scan direction) and largest part dimension.

3. In-plane tensile residual strains measured via neutron diffraction increase with proximity to the top surface of our AM parts, causing them to deform spherically with the edges "peeling up" upon sectioning/build plate removal. We attribute this behavior to constraint against in-plane shrinkage imposed by sub-surface layers, coupled with reheating effects of the sub-surface layers.
4. Investigations into the coupled effect of laser power and speed reveal that as energy per unit length is increased, residual stress induced deflection upon sectioning is decreased. These processing parameters have multiple effects, including altering the temperature of the substrate/sub-surface layer and the size of the heat affected zone. These results indicate that increasing both of these results in lower residual stresses in powder bed fusion parts.

Acknowledgments

This work was performed under the auspices of the U.S. Department of Energy by Lawrence Livermore National Laboratory under Contract DE-AC52-07NA27344. This work was funded by the Laboratory Directed Research and Development Program at LLNL under project tracking code 13-SI-002.

The authors would like to acknowledge the guidance and expertise of Ms. Mary M. LeBlanc (LLNL) in mechanical characterization techniques and digital image correlation methodology. Dr. Bjørn Clausen and Dr. Thomas A. Sisneros (LANL, Lujan Center) are recognized for their time and expertise in neutron diffraction. The authors also recognize Dr. Bassem el-Dasher, Dr. Robert Ferencz and Dr. Neil Hodge (LLNL) for their guidance in planning these experiments—and, in particular, Dr. Neil Hodge for melt pool geometry predictive capabilities, as well as Dr. Chandrika Kamath (LLNL) for process optimization expertise and Dr. John Elmer (LLNL) for his advice and expertise. Mr. Gregory J. Larsen and Mr. Paul Alexander are recognized for their drafting efforts and processing expertise, respectively. Dr. Karl Fisher provided the resonance ultrasound spectroscopy measurements of elastic modulus used in this study.

References

1. I. Gibson, D.W. Rosen, B. Stucker: Additive manufacturing technologies: Rapid prototyping to direct digital manufacturing, Springer, New York, NY, 2010.
2. S.H. Huang, P. Liu, A. Mokasdar, L. Hou: International Journal of Advanced Manufacturing Technology, 2013, vol. 67, pp. 1191-1203.
3. D.D. Gu, W. Meiners, K. Wissenbach, R. Poprawe: International Materials Reviews, 2012, vol 57, pp. 133-164.
4. R. Felzmann, S. Gruber, G. Mitteramskogler, P. Tesavibul, A.R. Boccaccini, R. Liska, J. Stampfl: Advanced Engineering Materials, 2012, vol. 14, pp. 1052-1058.
5. N. Travitzky, A. Bonet, B. Dermeik, T. Fey, I. Filbert-Demut, L. Schlier, T. Schlordt, P. Greil: Advanced Engineering Materials, 2014, DOI: 10.1002/adem.201400097
6. P. Mercelis and J.-P. Kruth: Rapid Prototyping Journal,2006, vol. 12, pp. 254-265.
7. C.R. Knowles, T.H. Becker, R.B. Tait: South African Journal of Industrial Engineering, 2012, vol. 23, pp. 119-129.
8. M.F. Zaeh, G. Branner: Prod. Eng. Res. Devel., 2010, vol. 4, pp. 35-45.
9. J.P. Kruth, J. Deckers, E. Yasa, R. Wauthlé: Proceedings of the Institution of Mechanical Engineers, Part B: Journal of Engineering Manufacture, 2012, vol. 226, pp. 980-991.

10. E. Yasa: Manufacturing by combining selective laser melting and selective laser erosion/laser re-melting. Dissertation, Katholieke Universiteit Leuven, Belgium, 2011.
11. N.W. Klingbeil, J.L. Beuth, R.K. Chin, C.H. Amon: International Journal of Mechanical Sciences, 2002, vol. 44, pp. 57-77.
12. P. Aggarangsi, J.L. Beuth: Proceedings of the Annual International Solid Freeform Fabrication Symposium, Austin, Texas, 2006, pp. 709-720.
13. A. Vasinota, J.L. Beuth, M.L. Griffith: ASME Journal of Manufacturing Science and Engineering, 2007, vol. 129, pp. 101-109.
14. M. Shiomi, K. Osakada, K. Nakamura, T. Yamashita, F. Abe: CIRP Annals - Manufacturing Technology, 2004, vol. 53, pp. 195-198.
15. V. Hauk: Structural and residual stress analysis by nondestructive methods, Elsevier Science B.V. Amsterdam, The Netherlands, 1997.
16. P.J. Withers, H.K.D.H. Bhadeshia: Materials Science and Technology, 2001, vol. 17, pp. 355-365.
17. I.C. Noyan, T.C. Huang, B.R. York: Critical Reviews in Solid State and Materials Sciences, 1995, vol. 20, pp. 125-177.
18. D.W. Brown, T.M. Holden, B. Clausen, M.B. Prime, T.A. Sisneros, H. Swensen, J. Vaja: Acta Materialia, 2011, vol. 59, pp. 864-873.
19. M.E. Fitzpatrick, A. Lodini: Analysis of residual stress by diffraction using neutron and synchrotron radiation. Taylor & Francis, London, 2003.
20. D.I. Crecraft: Journal of Sound and Vibration, 1967, vol. 5, pp. 173-192.
21. D.D.L. Chung: Thermochemica Acta, 2000, vol. 364, pp. 121-132.
22. E.S. Gorkunov, S.M. Zadvorkin, L.S. Goruleva: 18th World Conference for Nondestructive Testing, 16-20 April, 2012, Durban, South Africa.
23. V. Sergo, G. Pezzotti, O. Sbaizero, T. Nishida: Acta Materialia, 1998, vol. 46, pp.1701-1710.
24. J.W. Ager III, M.D. Drory: Physical Review B, 1993, vol. 48, pp. 2601-2607.
25. K. Kusaka, T. Hanabusa, M. Nishida, F. Inoko: Thin Solid Films, 1996, vol. 290-291, pp. 248-253.
26. T. Kannengiesser, A. Kromm, M. Rethmeier, J. Gibmeier, C. Genzel: Advances in X-ray Analysis, 2009, vol. 52, pp. 755-762.
27. Y. Watanabe, M. Nishida, T. Hanabusa: Advances in X-ray Analysis, 2009, vol. 52, pp. 271-278.
28. ASTM Standard E837 REV A: Standard Test Method for Determining Residual Stresses by the Hole-Drilling Strain-Gage Method, ASTM International, West Conshohocken, PA, 2013
29. M.B. Prime: Journal of Engineering Materials and Technology, 2000, vol. 123, pp. 162-168.
30. M.B. Prime: Applied Mechanics Reviews, 1999, vol. 52, pp. 75-96.
31. D.V. Nelson, A. Makino, T. Schmidt: Experimental Mechanics, 2006, vol. 46, pp. 31-38.
32. J.D. Lord, D. Penn, P. Whitehead: Applied Mechanics and Materials, 2008, vol. 13-14, pp. 65-73.
33. J. Gao, H. Shang: Applied Optics, 2009, vol. 48, pp. 1371-1381.
34. A. Baldi: Experimental Mechanics, 2013, doi: 10.1007/s11340-013-9814-6
35. J. Zhu, H. Xie, Z. Hu, P. Chen, Q. Zhang: Surface & Coatings Technology, 2011, vol. 206, pp. 1396-1402.
36. N. Daynes, G. Horne, P.J. Heard, D.Z.L. Hodgson, A. Shterenlikht: Advances in X-ray Analysis, 2009, vol. 52: pp. 651-658.

37. A. M. Korsunsky, M. Sebastiani, E. Bemporad: Surface & Coatings Technology, 2010, vol. 205, pp. 2393-2403.
38. Y.S. Yang, J.G. Bae, C.G. Park: Journal of Physics: Conference Series, 2008, vol. 100, pp. 012018.
39. L. Bingleman, G.S. Schaker: Proceedings of the SEM Annual Conference, June 7-10, 2010, Indianapolis, USA.
40. J. Zhang: Optical Engineering, 1998, vol. 37, pp. 2402-2409.
41. O. Sedivy, C. Krempaszky, S. Holy: Australian Congress on Applied Mechanics, Dec. 10-12, 2007, Brisbane, Australia.
42. J. Zhang, W.C. Fok, T.C. Chong: Proc. SPIE 2921, International Conference on Experimental Mechanics: Advances and Applications, 1997, pp. 584-591.
43. S. Suresh, A.E. Giannakopoulos: Acta Materialia, 1998, vol. 46, pp. 5575-5567.
44. B. Vrancken, R. Wauthlé, J.-P. Kruth, J. Van Humbeeck: Proceedings of the Solid Freeform Fabrication Symposium, Aug. 12-14, 2013, Austin, Texas, pp.393-407.
45. C. Kamath, B. El-dasher, G.F. Gallegos, W.E. King, R. Lee, A. Sisto: International Journal of Advanced Manufacturing Technology (in press).
46. L. Thijs, M.L. Montero Sistiaga, R. Wauthle, Q.G. Xie, J.-P. Kruth, J. V. Humbeeck: Acta Materialia, 2013, vol. 61, pp. 4657-4668.
47. T. Niendorf, S. Leuders, A. Riemer, H.A. Richard, T. Tröster, D. Schwarze: Metallurgical and Materials Transactions B, 2013, vol. 44B, pp. 794-796.
48. J.A. Choren, S.M. Heinrich, M.B. Silver-Thorn MB: Journal of Materials Science, 2013, vol. 48, pp. 5103-5112.
49. H. Gu, H. Gong, D. Pal, K. Rafi, T. Starr, B. Stucker: Twenty Forth Annual International Solid Freeform Fabrication Symposium–An Additive Manufacturing Conference, Aug. 12-14, 2013, Austin, TX.
50. D.B. Hann, J. Iammi, J. Folkes: J. Phys. D: Appl. Phys., 2011, vol. 44, pp. 445401.
51. T.W. Eagar, N.S. Tsai: Welding Journal, 1983, vol. 62, pp. S346-S355.
52. R. Rai, J.W. Elmer, T.A. Palmer, T. DebRoy: J. Phys. D: Appl. Phys., 2007, vol. 40, pp. 5733-5766.
53. P. Bleys, J.-P. Kruth, B. Lauwers, B. Schacht, V. Balasubramanian, L. Froyen, J.V. Humbeek: Advanced Engineering Materials, 2006, vol. 8, pp. 15-25.
54. L. Wang, S.D. Felicelli, P. Pratt: Materials Science and Engineering A, 2008, vol. 496, pp. 234-241.

Table 1. Mechanical and physical properties of AM specimens processed at a laser power and speed of 400W and 1800mm/s as a function of scanning strategy

Processing Conditions	Elastic Modulus (GPa)		Yield Stress 0.2% offset (MPa)	Porosity (%)
	compression	RUS		
5x5 mm islands[a]	187[c]	190	422[d]	1.2±0.1
3x3 mm islands[a]		183	467[d]	1.3
3x3 mm islands[b]		184	437[d]	1.3
Continuous scanning		173	345[d]	5.1
Wrought	193	N/A	170	0

[a]x-y shift of 1 mm between layers
[b]x-y shift of 0.6 mm between layers
[c]Measurement acquired using three strain gages at 120º around the specimen diameter; experiment performed for the 5x5 mm case only
[d]Measured under compressive loading

Table 2. Porosity and calculated AM characteristics in specimens processed using the 5x5 mm island scanning strategy for specified function of laser settings

Processing Conditions	Porosity (%)	Energy/Unit Length (J/m)	Normalized Enthalpy	Melt Pool Width (µm)	Melt Pool Length (µm)	Melt Pool Depth (µm)
100W, 400mm/s	0.93	250	32.4	129.6	212.4	59.5
250W, 1500mm/s	0.9[a]	167	41.8	105.6	526.0	52.8
250W, 1800mm/s	1.39	139	38.2	100.8	523.5	48.0
400W, 1800mm/s	1.19±0.09	222	61.1	129.6	846.4	60.0

[a]From Kamath et al.[15]

Table 3. Laser parameters and AM specimen material properties

parameter	symbol	316L
Surface absorptivity	η	0.4
Power	P	variable
Density at melting	ρ	7978 kg/m^3
Enthalpy at melting	h_s	1.2 (10^6)[a] J
Thermal diffusivity	α	5.38 (10^{-6}) m^2/s
Half width of Gaussian beam at surface	σ	1.3 (10^{-5}) m
Speed	U	variable
Specific energy/kg	ΔH	variable

[a]From Rai et al.[52]

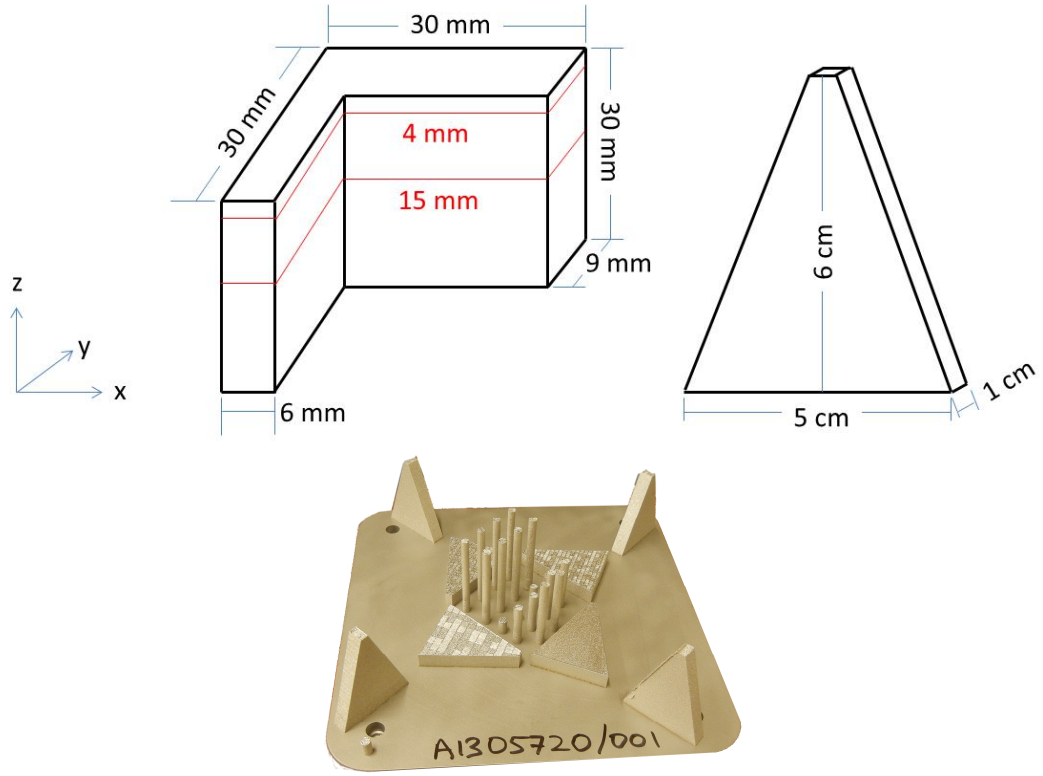

Fig. 1. Specimen schematic and dimensions and as-built horizontal and vertical prism specimens

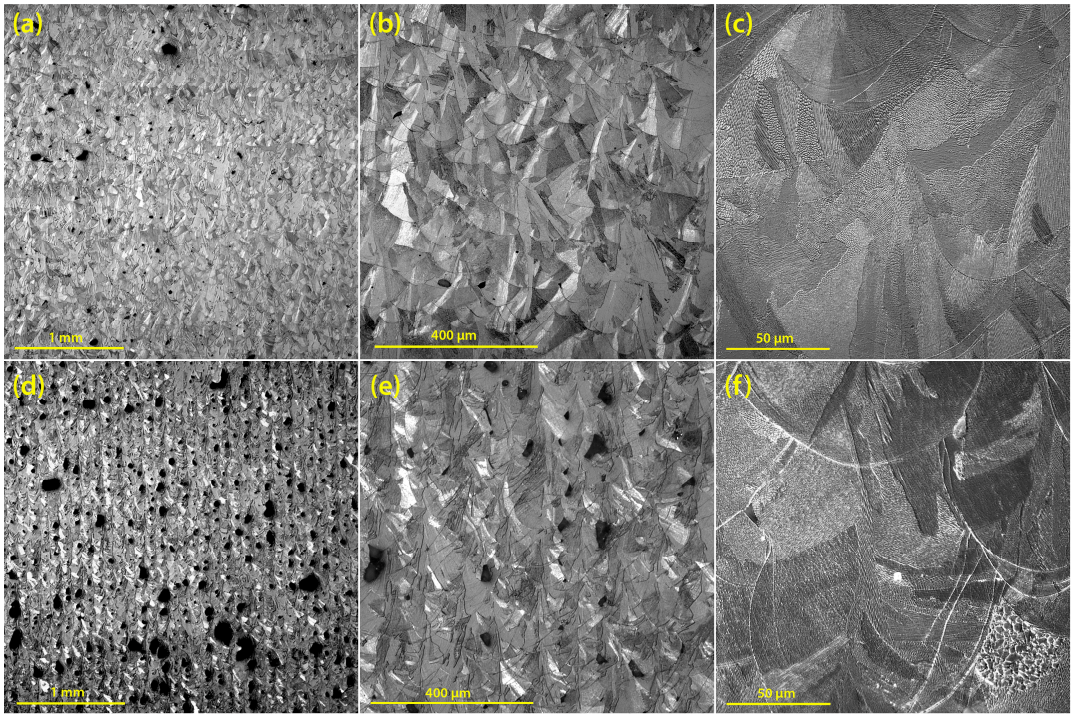

Fig. 2. Cross-sectional images (SEM) of (a)-(c) 5x5 mm island specimen and (d)-(f) continuously scanned specimen depicting grain structure and porosity processed at 400 W and 1800 mm/s

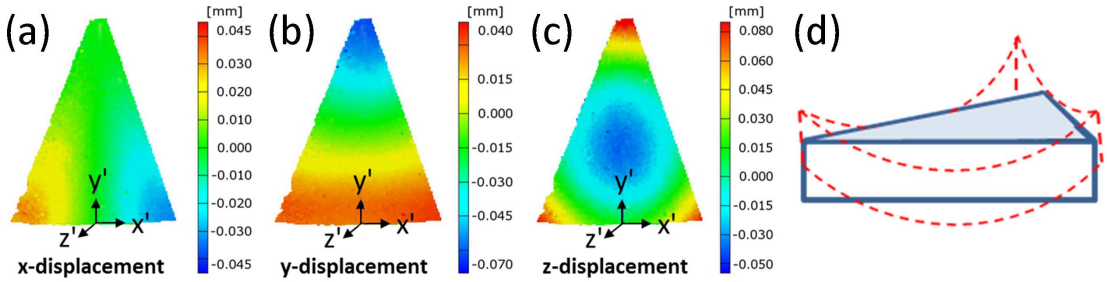

Fig. 3. (a)-(c) Top surface displacements with local (surface) coordinate system for horizontal specimens scanned using a 5x5 mm island pattern 0º from the base wall; (d) exaggerated deformation schematic

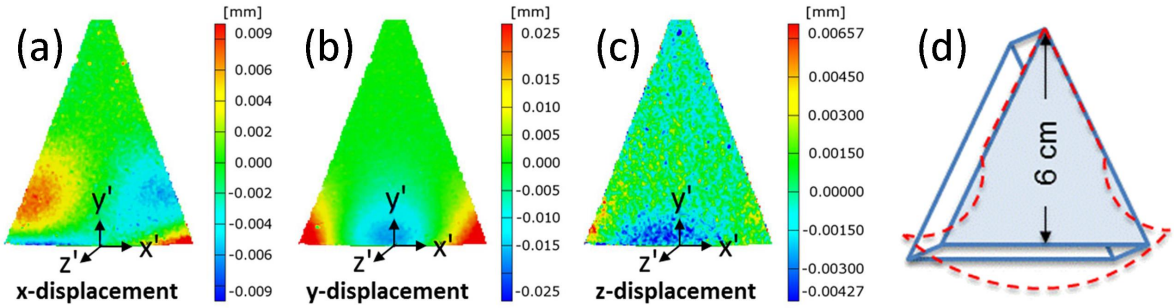

Fig. 4. (a)-(c) Side face displacements with local (surface) coordinate system for vertical specimens scanned using a 5x5 mm island pattern 0º from the base wall; (d) exaggerated deformation schematic

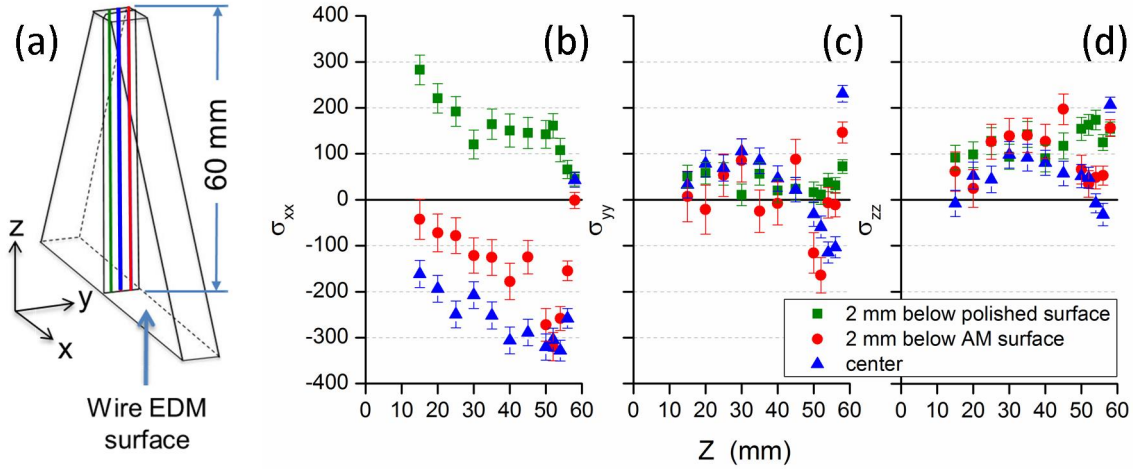

Fig. 5. Neutron diffraction measurements along (a) the axis of a vertically-built prism with one polished face yield residual stress components (b-d).

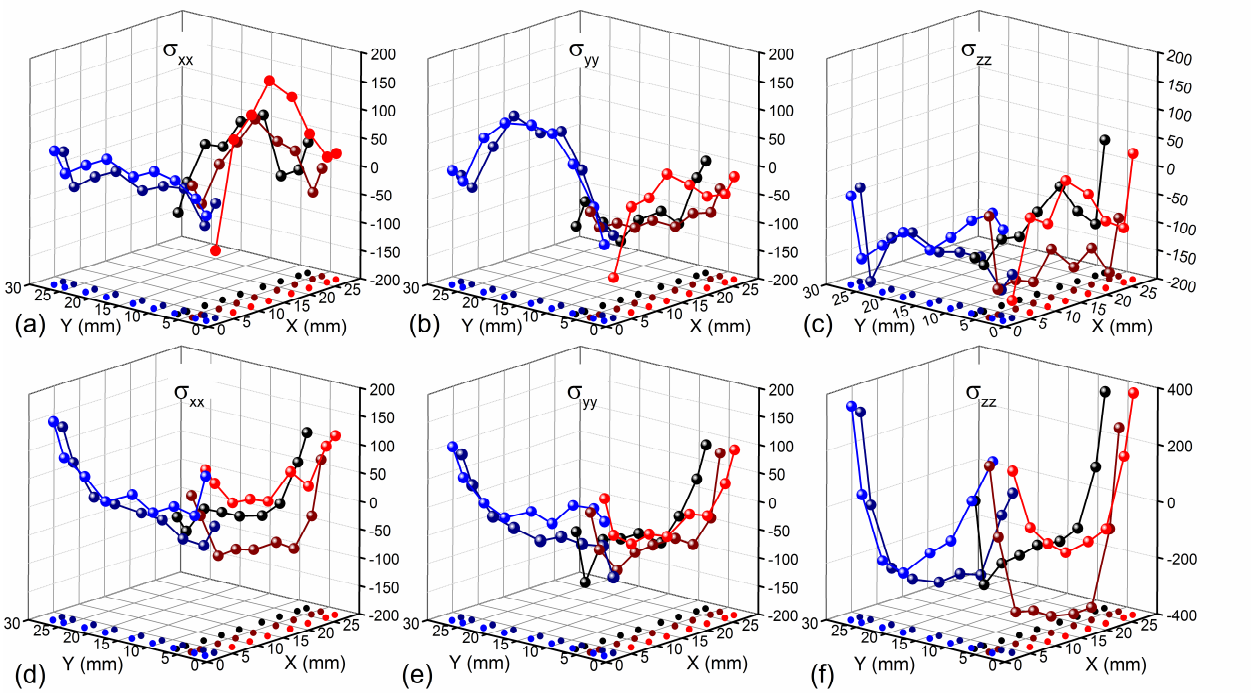

Fig. 6. Residual stress components measured via neutron diffraction at (a-c) 4 mm and (d-f) 15 mm from the top of the specimen. See Fig. 1 for coordinate system and neutron diffraction scan locations.

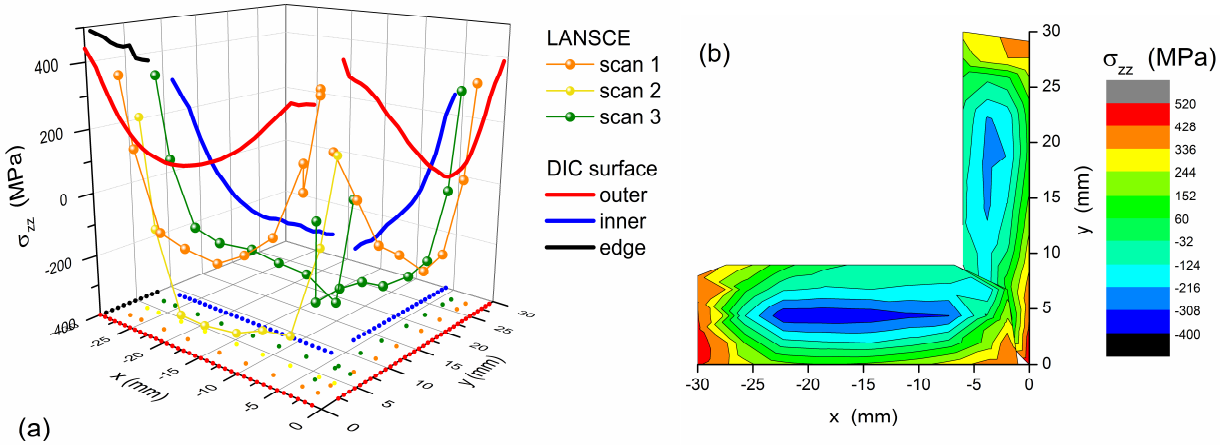

Fig. 7. Comparison of surface and volumetric axial residual stresses measured via DIC/sectioning and neutron diffraction, respectively, at z=15 mm in an L-shaped bracket specimen built at 400 W and 1800 mm/s shown as a (a) 3D and (b) contour plot

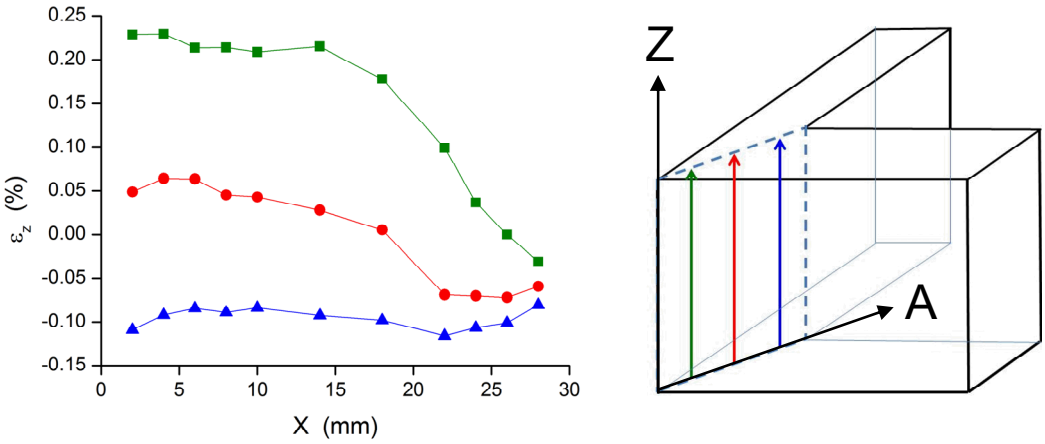

Fig. 8. Residual axial strains measured via neutron diffraction along the corner of an L-shaped bracket specimen built using 5 x 5 mm islands 45º off the part walls and a laser power and speed of 400W and 1800mm/s, respectively

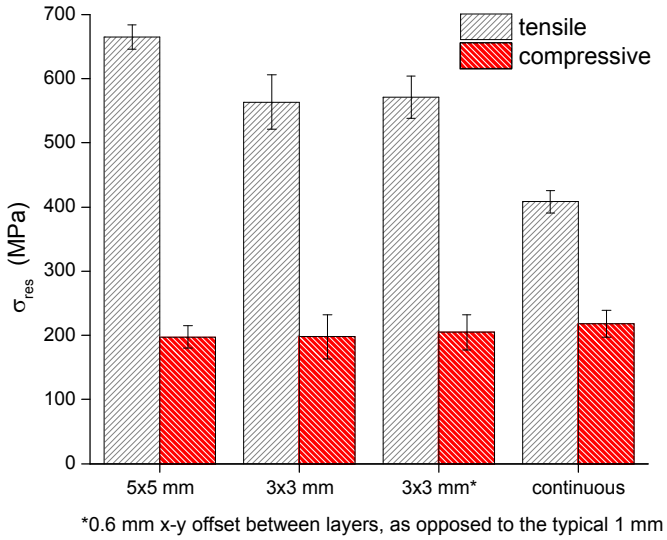

Fig. 9. Residual stresses in vertically-built AM parts are measured via DIC/sectioning and calculated based on RUS measured elastic moduli.

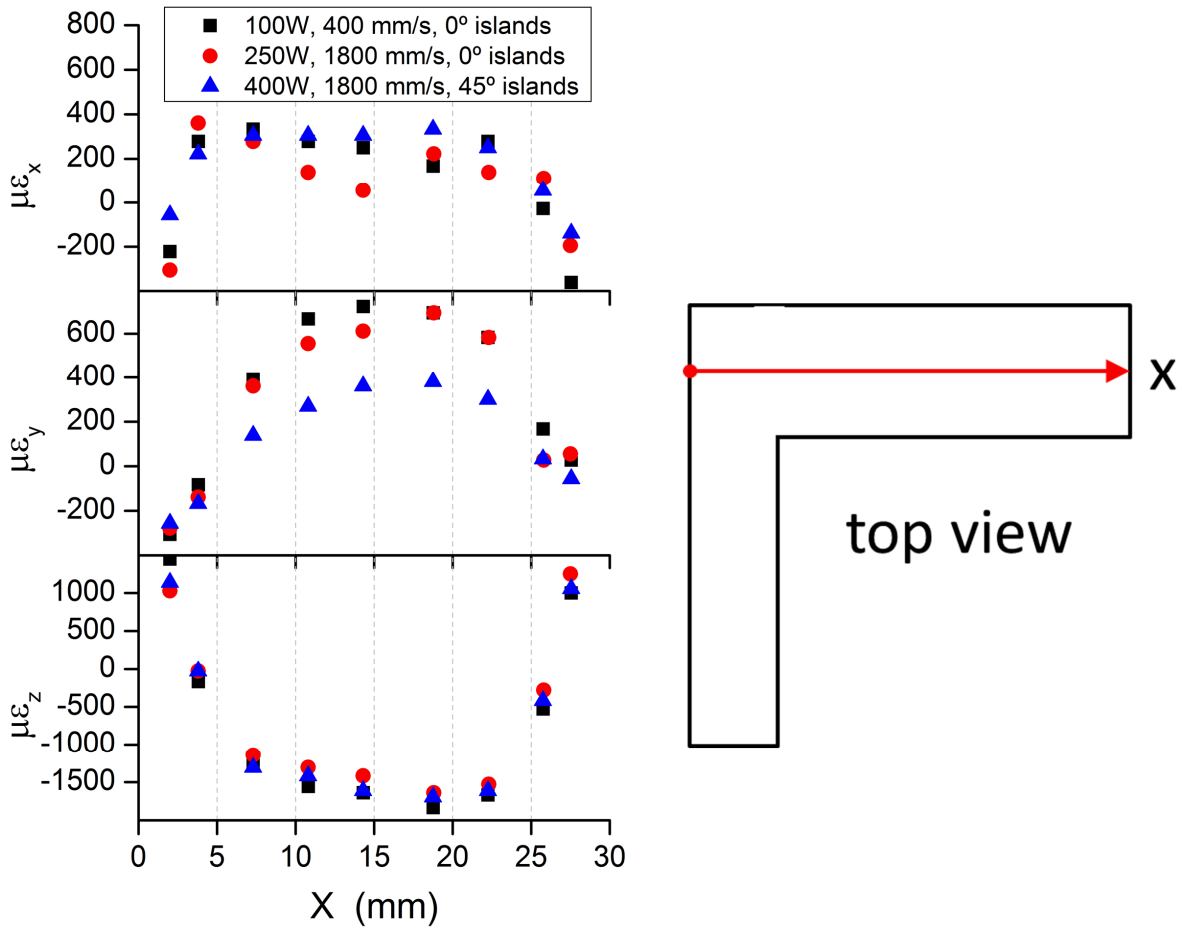

Fig. 10. Neutron diffraction measured residual strain components in an L-shaped specimen; measurements acquired at z=15 mm

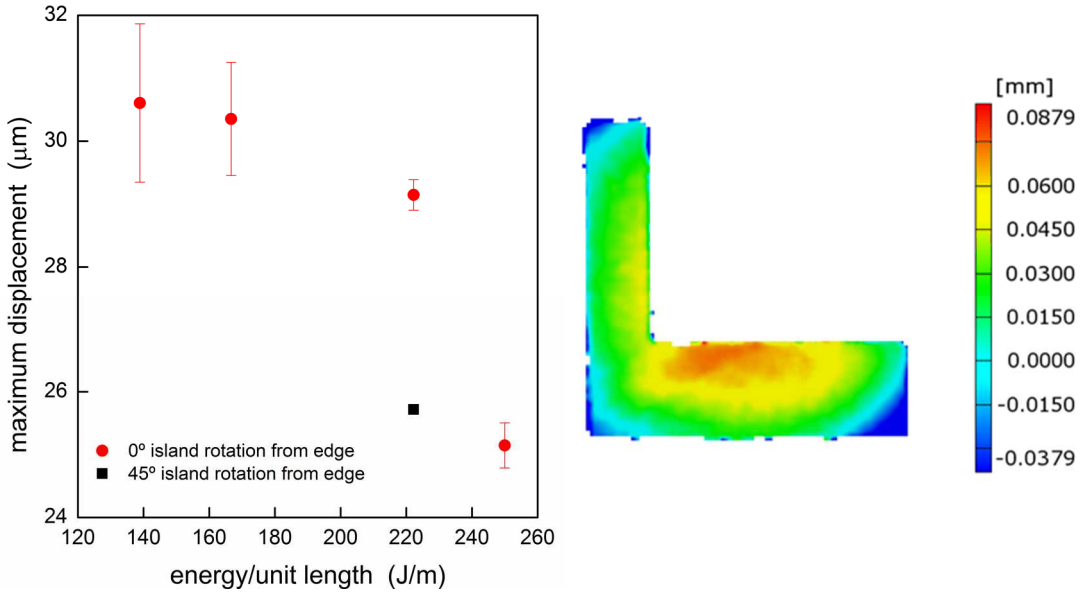

Fig. 11. Maximum center-to-corner surface axial displacement measured via DIC at z=15 mm